Chapter 2

Structural Characteristics and Thermal Properties of Native Cellulose

Matheus Poletto, Vinícios Pistor and Ademir J. Zattera

Additional information is available at the end of the chapter

http://dx.doi.org/10.5772/50452

1. Introduction

In 1838 the French chemist Anselme Payen discovered and isolated cellulose from green plants [1-2]. After more than 170 years of the discovery of the "sugar of the plant cell wall", consumers, industry and government are increasingly demanding products from renewable and sustainable resources that are biodegradable, non-petroleum based, carbon neutral and at the same time generating low environmental, animal/human health and safety risks [3]. Therefore, cellulose is one of the most abundant material on earth and the most common organic polymer, representing about 1.5 x 10^{12} tons of the annual biomass production [1,3]. Cellulose is considered an almost inexhaustible source of raw material for the increasing demand for environmentally friendly and biocompatible products. Therefore, wood remains one of the most important raw material source for obtaining cellulose, but other sources can be used as well. Natural cellulose-based materials (wood, hemp, cotton, sisal, ramie, etc.) have been used as engineering materials for thousands of years and their use currently continues as demonstrated by the huge number of forest products-based worldwide industries, such as paper, textiles, etc. Such cellulose derivatives produced on an industrial scale are used for coatings, laminates, optical films and sorption media, as well as for property-determining additives in building materials, composites and nanocomposites, pharmaceuticals, foodstuffs and cosmetics [2-3]. As a consequence, several reviews and scientific papers have been published on cellulose research in the last two decades [2-4].

At this time one question can be asked: what makes cellulose such an important material? The fascination for cellulose results from its specific structure. The cellulose macromolecule is made up of repeating glucose units that generate surprising specificity and impressively diverse architectures, reactivities and functions [2]. The reactions and properties of cellulose are determined by the isolation process used, the number of inter- and intramolecular hydrogen bonds, the chain lengths, the chain length distribution, the crystallinity and by the

distribution of functional groups within the repeating units and along the polymer chains [2, 5-6]. These important parameters make cellulose a unique material.

2. Structure of cellulose

Cellulose is a natural polymer consisting of ringed glucose molecules. The repeat unit showed in Figure 1 is comprised of two anhydroglucose rings $(C_6H_{10}O_5)_n$, linked together through an oxygen covalently bonded to the C1 of one glucose ring and the C4 of the adjoining ring (1 → 4 linkage) and so called the β 1-4 glucosidic bond [2-3]. The degree of polymerization, *n*, varies between 10 000 and 15 000, where *n* is dependent on the cellulose source material [3,7].

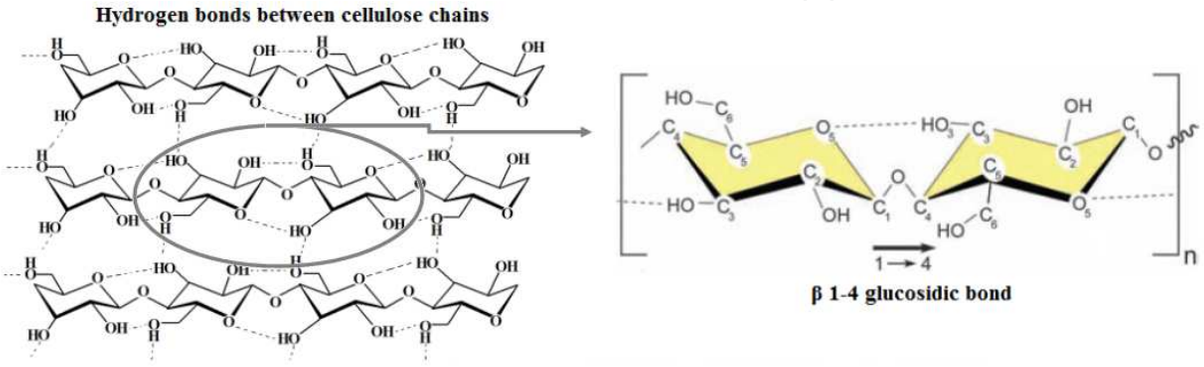

Figure 1. Molecular structure of a cellulose unit, showing the β 1-4 glucosidic bond and the intrachain hydrogen bonding (dotted line) (Adapted from [3]).

As can be seen in Figure 1, each repeating unit contains three hydroxyl groups. These hydroxyl groups and their ability to make hydrogen bonds between cellulose chains govern the physical properties of cellulose [7]. The intrachain hydrogen bonding between hydroxyl groups and oxygens of the adjoining ring molecules stabilizes the linkage and results in the linear configuration of the cellulose chain [3]. During cellulose formation, van der Waals and intermolecular hydrogen bonds between hydroxyl groups and oxygens of adjacent molecules promote aggregation of multiple cellulose chains forming fibrils [2-3]. The intra- and inter-chain hydrogen bonding network makes cellulose a relative stable polymer, and gives the cellulose fibrils high axial stiffness [3]. The high cohesive energy ensuing from these physic-chemical interactions explains why cellulose does not possess a liquid state [8] and these cellulose fibrils are the main reinforcement phase in trees and plants. Within these cellulose fibrils there are regions where the cellulose chains are arranged in a highly ordered crystalline structure and regions that are low order or amorphous regions [3,7].

2.1. Crystal structure

The polymorphy of cellulose and its derivatives has been well documented. These are cellulose I, II, III and IV [1-3]. Cellulose I, or native cellulose, is the form found in nature. Its structure is thermodynamically metastable and can be converted to either cellulose II or III [3,7]. This work focuses on the characterization of the cellulose I structure, which is the crystal structure naturally produced by a variety of organisms.

Cellulose I has two polymorphs, a monoclinic structure Iβ and a triclinic strucuture Iα, which coexist in various proportions depending on the cellulose structure [3,9]. The Iα is a rare form, whereas Iβ is the dominant polymorph for higher plants [10]. The Iα polymorph is metastable and can be converted into Iβ by hydrothermal treatments in alkaline solution [3,9].

The Iα and Iβ polymorph structures are shown in Figure 2. The Iα unit cell contains one cellulose chain, the unit cell parameters being a = 0.672 nm, b = 0.596 nm, c = 1.040 nm, α = 118.08°, β = 114.80°, γ = 80.375° [3]. The Iβ unit cell contains two cellulose chains, and the unit cell parameters are a = 0.778 nm, b = 0.820 nm, c = 1.038 nm, and γ = 96.5° [1,10]. Three lattice planes with approximate d-spacings of 0.39 nm, 0.53 nm and 0.61 nm correspond to the Iα lattice planes (110), (010), and (100) for the triclinic structure, and to the Iβ lattice planes (200), (110) and $(1\bar{1}0)$ for the monoclinic structure [3,9]. The main difference between the Iα and Iβ polymorph structures is the relative displacement of cellulose sheets along the (110) lattice plane in the triclinic structure and the (200) lattice plane in the monoclinic structure, called "hydrogen-bonded" planes, in the chain axis direction [2-3]. In Iα there is a relative displacement of c/4 between each subsequent hydrogen-bonded plane, while for Iβ the displacement alternates between ± c/4 through van der Waals interactions [3,10].

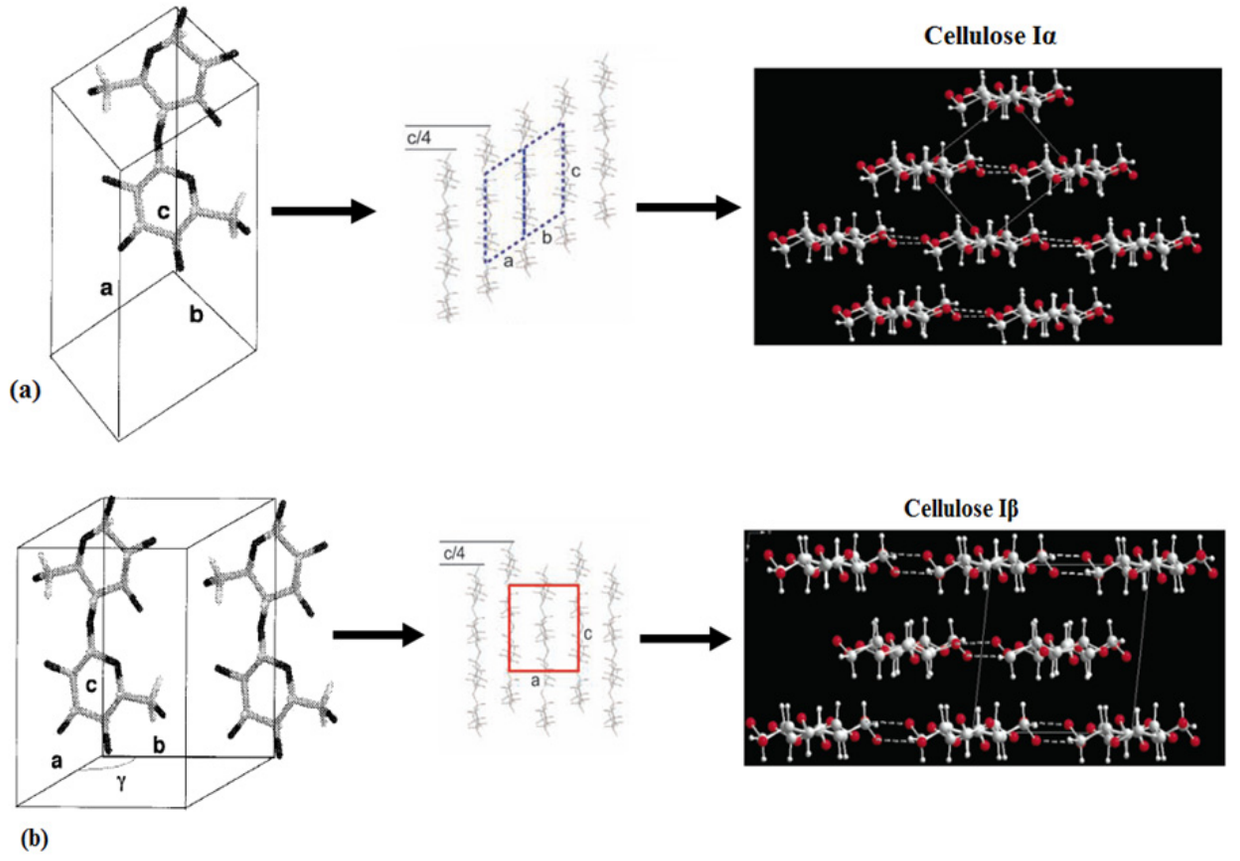

Figure 2. Schematic representation of the unit cells for cellulose structures Iα (a), and Iβ (b) and the displacement of the hydrogen bonding sheets for Iα of + c/4, and for Iβ alternating + c/4 and - c/4. (Adapted from [3, 11-12]).

2.2. Hydrogen bonding

Three hydroxyl groups are available for reaction in each repeating unit of cellulose, the structure of cellulose being largely affected by hydrogen bonds and van der Waals forces. Hydrogen bonding within neighboring cellulose chains may act to determine the straightness of the chain [1] and impart improved mechanical properties and thermal stability to the cellulose fibers. Interchain hydrogen bonds might introduce order or disorder into the system depending on their regularity [1].

So, understanding hydrogen bonding within the Iα and Iβ structures is important as it governs the stability and properties of these polymorphs [3] and of cellulose itself. With the hydroxyl groups being equatorial to the cellulose ring plane, intra- and inter-chain hydrogen bonding is most prevalent within the (110) plane in the triclinic structure and within the (200) plane in the monoclinic structure, hence the name " hydrogen-bonded" plane [3]. On the other hand, intrachain hydrogen bonding is dominated by strong O3-H···O5 bonds [1,3], as shown in Figure 1.

Inter-chain hydrogen bonding within the other planes (010), (100) in the triclinic structure and the planes (110) and ($1\bar{1}0$) in the monoclinic structure is substantially lower and attractive van der Waals forces are believed to dominate the cohesion forces between cellulose chains [3]. Within these planes the number of weak inter-chain hydrogen bonds in the Iβ structure is believed to be larger than in the Iα polymorph and it has been suggested that it would contribute to the higher stability of the Iβ form, as compared to the Iα form [3,9]. The Iα hydrogen bonds thermally degrade at lower temperatures, contributing to the lower Iα thermal stability [3].

In this way, this study focuses on the characterization of structure and thermal properties of cellulose I, sometimes referred to as native cellulose. This work investigates the relationship between chemical structure, hydrogen bond interactions, crystallite size and crystallinity and the influence of these parameters on the thermal stability and decomposition kinetics of cellulose fibers obtained by two different pulping processes. However, in order to better understand the parameters used in this work for cellulose characterization a brief theoretical background is presented.

3. Theoretical background

3.1. X-ray diffraction parameters

The *d*-spacings were calculated using the Bragg equation [10,13]:

$$n\lambda = 2dsen\theta \tag{1}$$

where n is the order of reflection, λ is the wavelength of the incident X-rays, d is the interplanar spacing of the crystal and θ is the angle of incidence. The crystalline index (Eq.2), proposed by Hermans et al. [13-14] is:

$$Cr.I. = \frac{A_{cryst}}{A_{total}} \quad (2)$$

where Cr.I. is the crystalline index, A_{cryst} is the sum of crystalline band areas, and A_{total} is the total area under the diffractograms.

The second approach used to determine the crystalline index (Eq. 3) was the empirical method proposed by Segal [13,15]:

$$Cr.I. = \frac{I_{200} - I_{am}}{I_{200}} \times 100 \quad (3)$$

where I_{200} is the maximum intensity of the (200) lattice diffraction and I_{am} is the intensity diffraction at 18° 2θ degrees. The apparent crystallite size (L) (Eq. 4) was calculated using the Scherrer equation [14]:

$$L = \frac{K \times \lambda}{H \times \cos\theta} \quad (4)$$

where K is a constant of value 0.94, λ is the X-ray wavelength (0.1542 nm), H is the half-height width of the diffraction band and θ is the Bragg angle corresponding to the (200) plane. The surface chains occupy a layer approximately 0.57 nm thick so the proportion of crystallite interior chains [14,16] is:

$$X = \frac{(L - 2h)^2}{L^2} \quad (5)$$

where L is the apparent crystallite size for the reflection of plane (200), and h=0.57 nm is the layer thickness of the surface chain. In this study, the Z-function developed by [13] for determination of the crystalline monoclinic and triclinic structures of cellulose was used.

By employing discriminant analysis it is possible to categorize cellulose as belonging to the Iα or Iβ predominant form. The Z-value indicates whether cellulose is Iα or Iβ [9]. The function which discriminates between Iα or Iβ [9] is given by:

$$Z = 1693d_1 - 902d_2 - 549 \quad (6)$$

where d_1 is the d-spacing of the Iβ ($1\bar{1}0$) peak and d_2 is the d-spacing of the Iβ (110) peak.

Z>0 indicates that cellulose is rich in the Iα form and Z<0 indicates that Iβ is the predominant form.

3.2. Fourier Transform Infrared (FTIR) spectroscopy

The ratio between the heights of the bands at 1372 cm^{-1} and 2900 cm^{-1} proposed by Nelson and O'Connor as total crystalline index (TCI) [17] was used to evaluate the infrared (IR)

crystallinity ratio. The band at 1430 cm^{-1} is associated with the amount of crystalline structure of cellulose, while the band at 898 cm^{-1} is assigned to the amorphous region in cellulose [17]. The ratio between the areas of the bands at 1430 cm^{-1} and 898 cm^{-1} is used as a lateral order index (LOI) [17]. Considering the chain mobility and bond distance, the hydrogen bond intensity (HBI) of cellulose is closely related to the crystal system and the degree of intermolecular regularity, that is, crystallinity [6]. The ratio of the absorbance bands at 3400 and 1320 cm^{-1} was used to study the cellulose samples HBI. The energy of the hydrogen bonds E_H for the OH stretching band was calculated using equation 7 [18]:

$$E_H = \frac{1}{K}\left[\frac{(\nu_0 - \nu)}{\nu_0}\right] \tag{7}$$

where ν_0 is the standard frequency corresponding to free OH groups (3650 cm^{-1}), ν is the frequency of the bonded OH groups, and K is a constant ($1/K = 2.625 \times 10^2$ kJ).

3.3. Thermogravimetric analysis (TGA)

For a reaction occurring during a differential thermal analysis (DTA), the change in the sample heat content and thermal properties is indicated by a deflection or a derivative peak. If the reaction is carried out using different heating rates, the level of activation energy (E_a) associated with this phenomenon, and therefore, the position of the peak of the derivative or the gradient of the deflection of the thermogravimetric curve varies with the heating rate whereas other experimental conditions are kept constant. The cellulose thermal decomposition is complex and may involve many reactions. It is very difficult to obtain precise kinetic parameters, however thermogravimetric analysis (TGA) has been used in recent decades as a quick evaluation for thermal stability. However, for the better understanding of the kinetic parameters determination a theoretical background is presented below.

3.4. Degradation kinetics

Information on the kinetics of degradation can be obtained by different methods. Kinetic studies assume that the isothermal conversion rate, $d\alpha/dt$, is a temperature-dependent linear function while the conversion (α) is independent of the temperature function according to Equation (8) [19-21]:

$$\frac{d\alpha}{dt} = k(T) f(\alpha) \tag{8}$$

where $f(\alpha)$ is a function dependent on the mechanism of decomposition and k is the rate constant. Equation (8) represents the rate of conversion at constant temperature according to the concentration of reactants at a constant rate. In this study, the conversion rate α is defined by [19-21]:

$$\alpha = \frac{m_0 - m_t}{m_0 - m_f} \tag{9}$$

where m_0, m_f and m_t are the initial and final weights of the sample and its weight at time (t), respectively.

The rate constant k is given by the Arrhenius equation [20-23]:

$$k = A\exp\left(E_a/RT\right) \tag{10}$$

where A is the pre-exponential factor (independent of temperature), and E_a is the activation energy, T is the absolute temperature and R is the gas constant. By combining Equations (8) and (10) the relationship described by Equation (11) is obtained:

$$\frac{d\alpha}{dt} = Af(\alpha)\exp\left(E_a/RT\right) \tag{11}$$

Whenever the sample temperature is controlled by a heating rate constant ($\beta=dT/dt$), the degree of conversion can be analyzed as a function of temperature. In this case the temperature becomes dependent of time at a heating rate, β, and the rate of reaction can be rewritten as:

$$\frac{d\alpha}{dt} = \frac{d\alpha}{dT}\frac{dT}{dt} = \beta\frac{d\alpha}{dT} \tag{12}$$

By considering the heating rate, again we can rewrite Equation (11) using the relationship shown in Equation (12), as shown in Equation (13):

$$\frac{d\alpha}{dT} = \frac{A}{\beta}e^{-\frac{E_a}{RT}}f(\alpha) \tag{13}$$

Integrating Equation (13) considering the initial temperature (T_0) and the initial conversion (α_0=0), we have:

$$\int_{\alpha_0}^{\alpha_\infty}\frac{d\alpha}{f(\alpha)} = \frac{A}{\beta}\int_{T_0}^{T_\infty}e^{\frac{E_a}{RT}}dT \tag{14}$$

Considering that T_0 is low and assuming $\alpha_0 = 0$ and that no reaction occurs between 0 and T_0:

$$g(\alpha) = \int_{0}^{\alpha_\infty}\frac{d\alpha}{f(\alpha)} = \frac{A}{\beta}\int_{T_0}^{T_\infty}e^{\frac{E_a}{RT}}dT \tag{15}$$

where $g(\alpha)$ is the integral function of conversion.

The degradation process can follow sigmoidal and deceleratory functions. These functions are shown in Table 1 through different $g(\alpha)$ expressions for the different solid state mechanisms [20, 22-23].

Mechanism	$g(\alpha)$	$f(\alpha)$
A_2, Nucleation and growth (Avrami equation (1))	$[-\ln(1-\alpha)]^{1/2}$	$2(1-\alpha)[-\ln(1-\alpha)]^{1/2}$
A_3, Nucleation and growth (Avrami equation (2))	$[-\ln(1-\alpha)]^{1/3}$	$3(1-\alpha)[-\ln(1-\alpha)]^{2/3}$
A_4, Nucleation and growth (Avrami equation (3))	$[-\ln(1-\alpha)]^{1/4}$	$4(1-\alpha)[-\ln(1-\alpha)]^{3/4}$
R_1, Controlled reaction on the surface (motion in one dimension)	α	1
R_2, Controlled surface reaction (dimensional contraction)	$[1-\ln(1-\alpha)^{1/2}]$	$2(1-\alpha)^{1/2}$
R_3, Controlled reaction on the surface (migration volume)	$[1-\ln(1-\alpha)^{1/3}]$	$3(1-\alpha)^{2/3}$
D_1, Diffusion in one dimension	α^2	$(1/2)\alpha^{-1}$
D_2, Diffusion in two dimensions (Valensi equation)	$(1-\alpha)\ln(1-\alpha)+\alpha$	$-[\ln(1-\alpha)]^{-1}$
D_3, Diffusion in three dimensions (Jander equation)	$[1-(1-\alpha)^{1/3}]^2$	$(3/2)[1-(1-\alpha)^{1/3}]^{-1}(1-\alpha)^{2/3}$
D_4, Diffusion in three dimensions (Ginstling–Brounshtein equation)	$[1-(2/3)\alpha]-(1-\alpha)^{2/3}$	$(3/2)[1-(1-\alpha)^{1/3}]^{-1}$
F_1, Random nucleation with one nucleus of individual particle	$-\ln(1-\alpha)$	$1-\alpha$
F_2, Random nucleation with two nuclei of individual particles	$1/(1-\alpha)$	$(1-\alpha)^2$
F_3, Random nucleation with three nuclei of individual particles	$1/(1-\alpha)^2$	$(1/2)(1-\alpha)^3$

Table 1. Expressions for $g(\alpha)$ and $f(\alpha)$ for the most frequently used mechanisms of degradation processes.

The mechanisms presented in Table 1 are essentially separated into four different groups shown schematically in Figure 3. The nucleation and growth (A_n) and random nucleation (F_n) are the most common types of mechanisms. Nucleation occurs through the breaking of bonds between molecules within the structure followed by rearrangement to release one molecule of product gas and a molecule referred to as the solid core of reaction [24]. The degradation reaction through nucleation is random, however, the speed of the degradation reaction tends to rise due to the fact that the formation of cores increases the concentration of degradation sites propagating along the material structure.

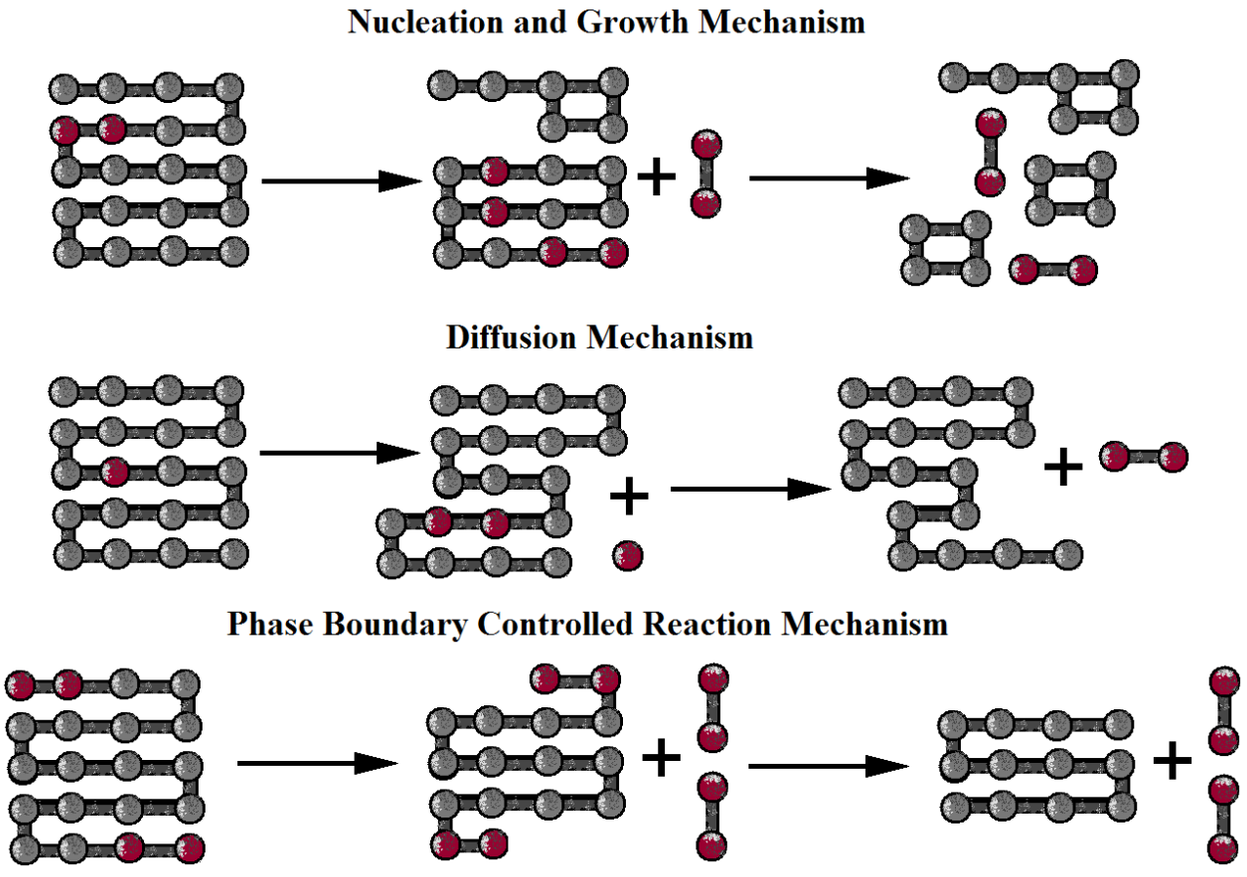

Figure 3. Schematic representation of the degradation processes reported by the mechanisms described in Table 1.

There are also controlled reactions at the interface (R_n). In mechanisms such R_n, degradation occurs from one end to the other one across the structure and this kind of mechanism is associated with the drawback of random breaking of bonds within the material structure. Factors that influence the material to follow the R_n mechanism are: high packing factor, molecular crosslinking and strong intermolecular interactions like hydrogen bonds between chains. Another class, diffusion (D_n), depends on the presence of one or more products formed by reaction or formation of gaseous products able to diffuse across the solid structure. Furthermore, in the case of macromolecules, the diffusion process becomes also dependent on the free volume and therefore the lower crystallinity and molecular packing factor can contribute for the degradation mechanism to occur by diffusion.

3.5. Flynn-Wall-Ozawa (FWO) method

In the FWO method [25-26], Equation (13) is integrated with the Doyle [27] approach and the result of the integration under logarithmic form is illustrated in Equation (16):

$$\log \beta = \log\left(\frac{AE_a}{g(\alpha)R}\right) - 2.315 - \frac{0.457E_a}{RT} \tag{16}$$

Using the FWO equation, the activation energy (E_a) can be determined for each fraction of conversion (α) required. The isoconversional FWO method assumes that the reaction rate at a given conversion (α) is a function of temperature only. Therefore, through different values of the temperature (T) it is possible to observe a linear relationship by plotting *log β vs. 1/T* x 10^{-3}. By linear fit the apparent activation energy (E_a) of degradation can be determined by the slope of the straight line obtained, where, *slope=(0.457 E_a/R)* [25-26].

3.6. Kinetic mechanisms of degradation

The activation energy of a solid state reaction can be determined, no matter the mechanism of degradation, by different methods, isothermal or non-isothermal. After determining the E_a, the mechanism of degradation can be estimated by the method proposed by Criado *et al*. [28] through the Z(α) function described in Equation (17):

$$Z(\alpha) = \frac{\left(d\alpha / dt\right)}{\beta} \pi(x) T \tag{17}$$

where x = (E_a/RT) and $\pi(x)$ is an integral function obtained by approximations and can not be obtained as an algebraic function. However, a relationship between π(x) and the function $P(x)$ can be assessed by the following expression proposed in Equation 18:

$$\pi(x) = xe^{x} P(x) \tag{18}$$

For the P(x) function, Senum and Yang's [29], proposed expressions of rotational 2nd and 4th degree to assess the accuracy of the integral of Arrhenius and ensure a margin of error precisely controlled. These expressions, to the 8th degree, are illustrated in Table 2. Using the expression of the 4th degree one can assume that for x > 20 the expression results in rotational errors of less than 10^{-5}% [29].

By combining Equations (8), (17) and (18) one can obtain the relationship shown in Equation (19):

$$Z(\alpha) = f(\alpha) g(\alpha) \tag{19}$$

Equation 19 allows the determination of the thermogravimetric master curves represented by the g(α) and f(α) functions as shown in Table 1. To confront the theoretical curves shown in Table 1, it is possible to superimpose the experimental data determined by Equation (20):

$$Z(\alpha) = \frac{d\alpha}{dT} \frac{E_a}{R} e^{\frac{E_a}{RT}} P(x) \tag{20}$$

So, Equation (19) is used to plot the master Z(α) versus α curves for the different models listed in Table 2, whereas Equation (20) is used to represent the experimental curve. By comparing these two curves, the kind of mechanism involved in the thermal degradation can be identified.

Degree $P(x)$	
1º	$\frac{\exp(-x)}{x}\frac{1}{x+2}$
2º	$\frac{\exp(-x)}{x}\frac{x+4}{x^2+6x+6}$
3º	$\frac{\exp(-x)}{x}\frac{x^2+10x+18}{x^3+12x^2+368x+24}$
4º	$\frac{\exp(-x)}{x}\frac{x^3+18x^2+86x+96}{x^4+20x^3+120x^2+240x+120}$
5º	$\frac{\exp(-x)}{x}\frac{x^4+28x^3+246x^2+756x+600}{x^5+30x^4+300x^3+1200x^2+1800x+720}$
6º	$\frac{\exp(-x)}{x}\frac{x^5+40x^4+552x^3+3168x^2+7092x+4300}{x^6+42x^5+630x^4+4200x^3+12600x^2+15120x+5040}$
7º	$\frac{\exp(-x)}{x}\frac{x^6+54x^5+1070x^4+9720x^3+41112x^2+71856x+35280}{x^7+56x^6+1176x^5+11760x^4+58800x^3+141120x^2+141120x+40320}$
8º	$\frac{\exp(-x)}{x}\frac{x^7+70x^6+1886x^5+24920x^4+170136x^3+577584x^2+844560x+357120}{x^8+72x^7+2024x^6+28560x^5+216720x^4+880320x^3+1794240x^2+1572480x+403200}$

Table 2. Expressions for one to eight degrees rational approximations for the Arrhenius integral.

4. Experimental

4.1. Materials

Bleached sulfite cellulose fibers from *Pinus taeda* (CPT) were supplied by Cambará S.A (Cambará do Sul, Brazil) obtained at the cooking temperature of 140°C and bleaching with hydrogen peroxide. Bleached kraft cellulose fibers from *Eucalyptus grandis* (CEG) were supplied by CMPC S.A. (Guaíba, Brazil), obtained at the cooking temperature of 155°C and bleaching with hydrogen peroxide. The samples were dried at 70°C for 24h in a vacuum oven before the tests. The average fiber particle length for both CTP and CEG is around 150 μm.

4.2. Methods

The X-ray diffractograms were collected using a sample holder mounted on a Shimadzu diffractometer (XRD-6000), with monochromatic Cu Kα radiation (λ = 0.1542 nm), the generator operating at 40 kV and 30 mA. Intensities were measured in the range of $5 < 2\theta < 35$°C, typically with scan steps of 0.05°C and 2s/step (1.5° min^{-1}). Peak separations were carried out using Gaussian deconvolution.

Fourier transform infrared spectroscopy spectra were obtained using a Nicolet IS10- Thermo Scientific spectrometer. Samples of the finely divided celluloses (5 mg) were dispersed in a KBr matrix (100 mg) followed by compression to form pellets. The analysis was obtained in triplicate using 32 scans, from 4000 cm^{-1} to 400 cm^{-1}, at a resolution of 4 cm^{-1}.

Thermogravimetric analysis (TGA50 – Shimadzu) was carried out under N_2 atmosphere, from 25 up to 600°C. Approximately 10 mg of each sample was used. The analysis was carried out at four different heating rates (5, 10, 20 and 40 °C min^{-1}). The results obtained were used to calculate the kinetic parameters.

5. Results and discussion

5.1. X-ray diffraction

X-ray diffraction is a method used generally to evaluate the degree of crystallinity of several materials. The free hydroxyl groups present in the cellulose macromolecules are likely to be involved in a number of intramolecular and intermolecular hydrogen bonds, which may give rise to various ordered crystalline arrangements [14, 21].

Figure 4 shows the X-ray diffractograms of the cellulose samples studied. In order to examine the intensities of the diffraction bands, establish the crystalline and amorphous areas more exactly and determine the crystallite sizes the diffractograms were deconvoluted using Gaussian profiles. Crystallographic planes are labeled according to the native cellulose structure as described by Wada et al. (2001) [30].

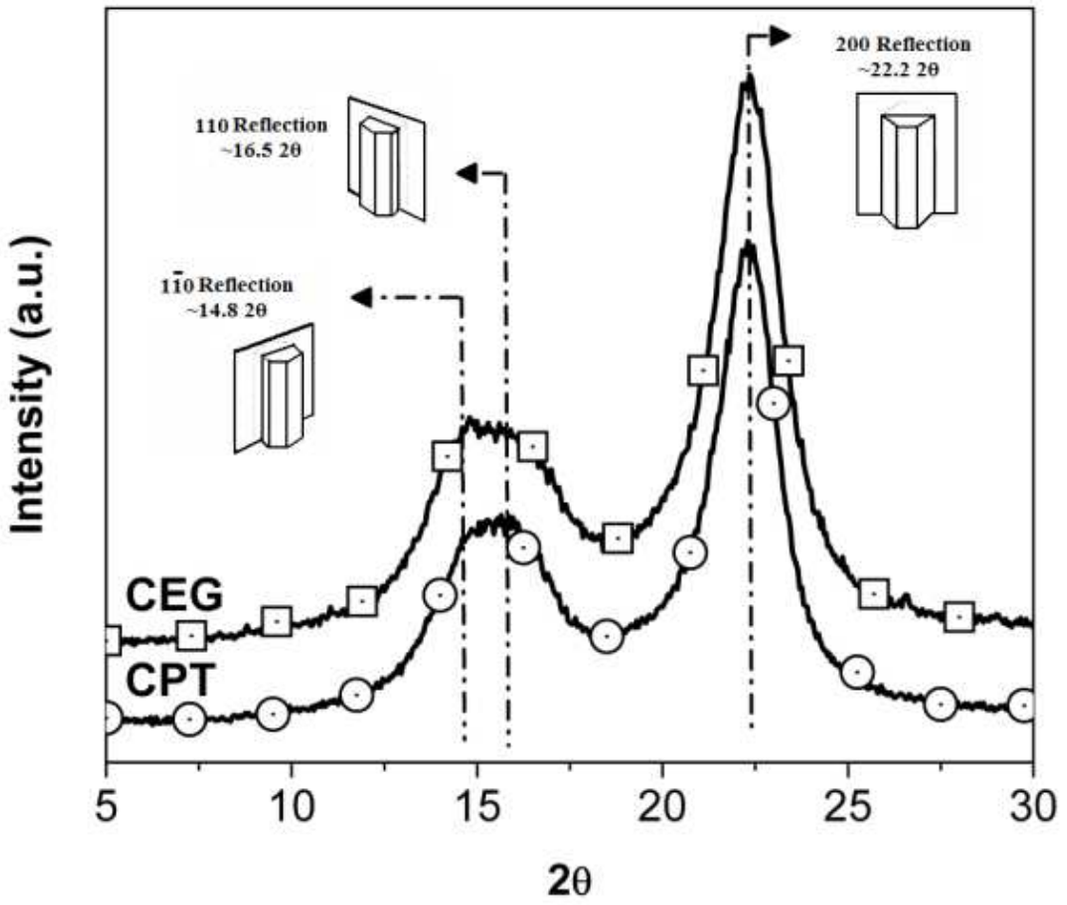

Figure 4. X-ray diffractograms of celluloses studied and corresponding crystal planes, adapted from [31], and most common 2θ values.

Following deconvolution, the two diffractograms show the 14.3-14.6°C 2θ reflection assigned to the ($1\bar{1}0$) crystallographic plane, the 16.00°C 2θ reflection assigned to the (110) crystallographic plane, the 18.30-18.40°C 2θ reflection assigned to the amorphous phase and the 22.20-22.40°C 2θ reflection assigned to the (200) crystallographic plane [14,30]. In Figure 5 a model is shown to represent the cellulose chains and the crystallographic planes described above.

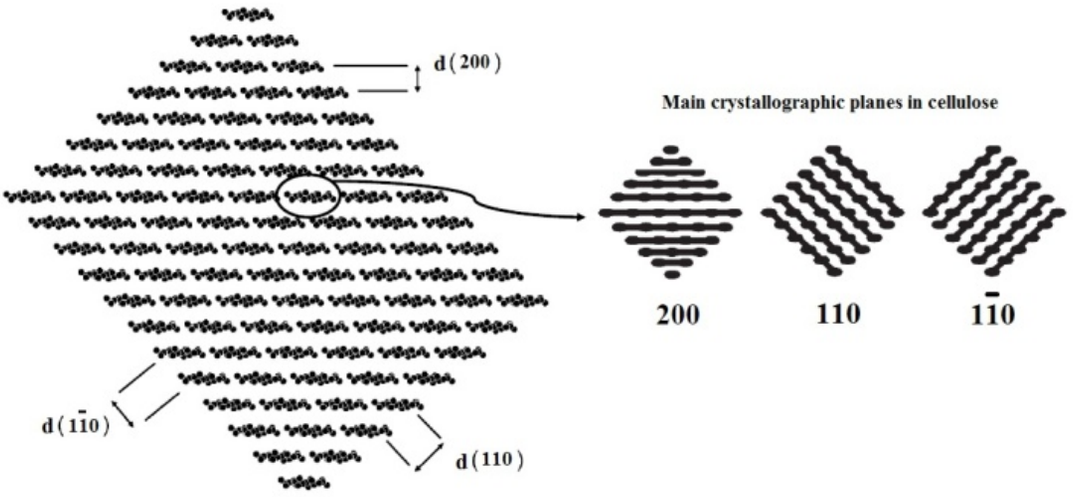

Figure 5. Model to represent cellulose chains (left), showing the d-spacings along the cellulose structure, adapted from [32]. Lines indicate the crystallographic planes in native cellulose (right), each circle on the line representing a chain normal to the paper, adapted from [33].

The band position (2θ values) and d-spacings of the celluloses calculated from X-ray diffractograms profiles are depicted in Table 2. Values of band position and d-spacings were similar.

Samples	($1\bar{1}0$)		(110)		Amorphous	(200)	
	2θ	d (nm)	2θ	d (nm)	2θ	2θ	d (nm)
CEG	14.30	0.618	16.00	0.553	18.30	22.40	0.397
CPT	14.60	0.605	15.95	0.555	18.40	22.20	0.399

Table 3. Band position (2θ) and d-spacings of crystalline and amorphous cellulose regions for the samples studied.

The degree of cellulose crystallinity is one of the most important crystalline structure parameters. The rigidity of cellulose fibers increases and their flexibility decreases with increasing ratios of crystalline to amorphous regions [15]. The crystallinity index calculated according to the Hermans (Eq. 2) and Segal methods (Eq. 3) showed that the CPT crystallinity is higher than that of CEG, as presented in Table 3. These differences are confirmed when the values of the crystallite size along the three crystallographic planes are taken into consideration. Crystallinity indices increased with increasing crystallite sizes because the crystallites surface corresponding to amorphous cellulose regions diminished

[10]. The values of *X* were used as estimates of the fraction of cellulose chains contained in the interior of the crystallites [33]. The proportion of crystallite interior chains, X, is similar for both samples. As can be seen in Table 3, the Z-values for CEG and CPT indicate that the cellulose samples belong to the Iβ dominant type, because Z<0 indicates that Iβ is the predominant form [9,13].

The crystallinity index (CrI) shows slight differences in crystallinity between the two cellulose samples. However, the d-spacing value for CPT in ($1\bar{1}0$) was around 20% higher than for CEG. The increase in the crystallite size for CPT in ($1\bar{1}0$), might be associated with a reduction in the corresponding amorphous region [10, 33]. If the amorphous domains of cellulose are attacked during the pulping treatment, chain scission and peeling reactions can occur, which reduce the total amount of amorphous regions and therefore increase the CPT crystallite size.

Samples	L ($1\bar{1}0$) (nm)	L (110) (nm)	L (200) (nm)	Cr.I.	C.I.	X	Z-values
CEG	3.783	2.370	3.826	60.4	74.9	0.493	-1.532
CPT	4.731	2.370	3.825	62.6	75.5	0.493	-25.345

Table 4. Parameters obtained from the XRD analysis of the cellulose samples studied.

These results confirm that CPT contains more cellulose chains in a highly organized form than CEG. This can lead to higher hydrogen bond intensity among neighboring cellulose chains resulting in a more packed cellulose structure besides higher crystallinity. On the other hand, the thermal stability of cellulose was found to depend mainly on its crystallinity index, crystallite size and degree of polymerization [10, 21, 33].

5.2. FTIR spectroscopy

FTIR spectroscopy has been used as a simple technique for obtaining rapid information about the chemical structure and crystallinity of cellulose samples [34-37]. Contrary to conventional chemical analysis, this method requires small sample sizes and short analysis time, besides being non-destructive [14].

Because of their complexity, the spectra were separated into two regions, namely: the OH and CH stretching vibrations in the 4000-2700 cm^{-1} region, showed in Fig. 6(a), and the "fingerprint" region which is assigned to different stretching vibrations of different groups in the 1800-800 cm^{-1} region, Figure 6(b). In Fig. 6(a) a strong broad band can be observed in the region of 3700-3000 cm^{-1} which is assigned to different OH stretching modes and another band in the region of 3000-2800 cm^{-1} is ascribed to the stretching of asymmetric and symmetric methyl and methylene cellulose groups [37]. The band at around 3360 cm^{-1} related to OH stretching modes is more prominent for CPT than for CEG. This is probably due to a larger number of hydroxyl groups in CPT which may be associated with an increase in the number of hydrogen bonds formed [14]. Thus, a mixture of intermolecular

and intramolecular hydrogen bonds is considered to cause the broadening of the OH band in the IR spectra [14].

Fig. 6(b) shows that in the "fingerprint" region the spectra revealed several bands. The band at 1642 cm^{-1} is associated with adsorbed water in cellulose and probably some hemicelluloses [17, 37-38]. The bands at 1430, 1370, 1335 and 1320 cm^{-1} are attributed to CH_2 symmetric bending, CH bending, in-plane OH bending, CH_2 rocking vibration, respectively [17, 38-39], and the bands at 1162, 1111, 1057, 1033, 898 cm^{-1} are assigned to asymmetric C-O-C bridge stretching, anhydroglucose ring asymmetric stretching, C-O stretching, in-plane C-H deformation and C-H deformation of cellulose, respectively [17, 38-41].

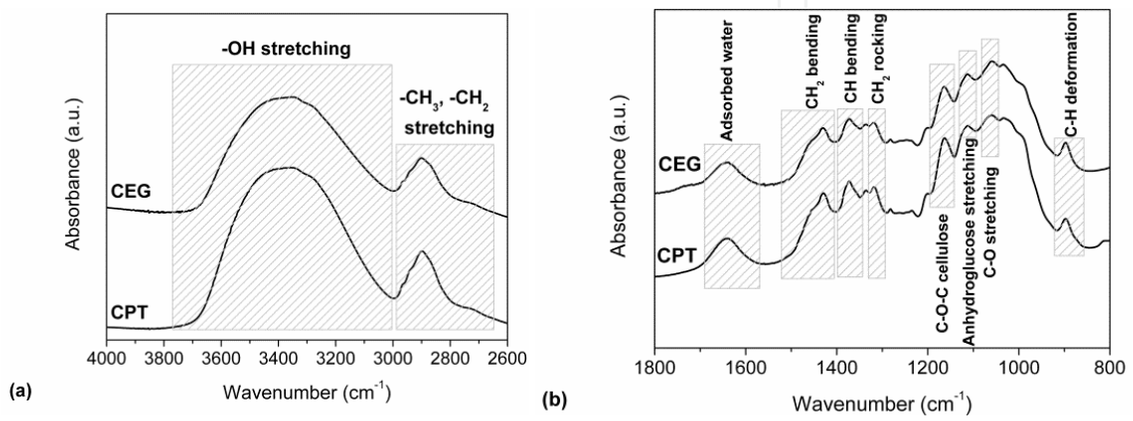

Figure 6. FTIR spectra of celluloses studied in the region between 4000-2800 cm^{-1} (a) and between 1800-800 cm^{-1} (b).

The total crystalline index (TCI), lateral order index (LOI), hydrogen bond energy (E_H), and hydrogen bond intensity (HBI) were calculated from the spectra obtained from FTIR spectroscopy. The obtained results are presented in Table 4.

Samples	IR crystallinity ratio		E_H	HBI
	H1372/H2900 (TCI)	A1429/A897 (LOI)	kJ	A3400/A1320
CEG	0.457 ± 0.020	3.507 ± 0.344	21.133 ± 0.092	1.368 ± 0.014
CPT	0.491 ± 0.010	4.071 ± 0.128	21.630 ± 0.311	1.455 ± 0.002

Table 5. Cellulose infrared crystallinity ratios and hydrogen bond intensity

TCI is proportional to the crystallinity degree of cellulose [14] while LOI is correlated to the overall degree of order in cellulose [17,41]. Based on this fact, CPT showed the higher TCI and LOI value indicating higher degree of crystallinity and more ordered cellulose structure than CEG. On the other hand, for CEG the lower cellulose infrared crystallinity values may indicate that the structure of this cellulose is composed of a larger number of amorphous domains when compared with CPT. The hydrogen bond energy is higher in CPT than in CEG. This is probably associated with higher crystallinity in this sample, as observed in the XRD analysis, which leads to more hydrogen bonds and so higher

hydrogen bond energy. The HBI value is higher for CPT than for the CEG sample. This result might indicate that CPT contains much more cellulose chains in a highly organized form which can lead to higher hydrogen bond intensity between neighboring cellulose chains and result in a more packing cellulose structure and higher crystallinity than CEG. The crystallinity of cellulose is closely related to thermal stability [10, 21, 42]. Therefore, it is possible that cellulose samples of higher TCI, LOI and HBI might exhibit higher thermal stability.

5.3. Thermogravimetric analysis

Figure 7 shows the TGA and DTG curves of the two cellulose samples using a heating rate of 10°C min^{-1}. A small weight loss for both samples occurs between 40-70°C which is attributed to the removal of absorbed water in cellulose [20, 43]. As depicted in Figure 7(a), the CEG sample initiates a more pronounced degradation process at around 280°C while for CPT a more pronounced degradation process occurs at 292°C. The main decomposition step occurs in the range of 240°C to 370°C for CEG and 250°C to 375°C for CPT. In this stage the cleavage of the glycosidic linkages of cellulose reduces the polymerization degree leading to the formation of CO_2, H_2O and a variety of hydrocarbon derivatives [44].

According to Figure 7, differences in the decomposition profiles of the two cellulose samples indicate slight thermal stability differences for the samples. The DTG peaks were centered at 353°C and 360°C for CEG and CPT, respectively, as presented in Figure 7(b). The DTG curve for CPT was shifted to higher temperatures with increasing crystallite size. This behavior suggests that higher crystallite size celluloses have higher thermal stability. Kim *et al*. [10] studied different types of cellulose and noted an increase in the crystallite size promoted by higher thermal stability. Therefore, higher TCI, LOI and HBI celluloses have higher thermal stability probably due to a much higher amount of hydrogen bonds between cellulose chains that can lead to more ordered and packed cellulose regions, this in turn possibly increasing the thermal decomposition temperature of cellulose.

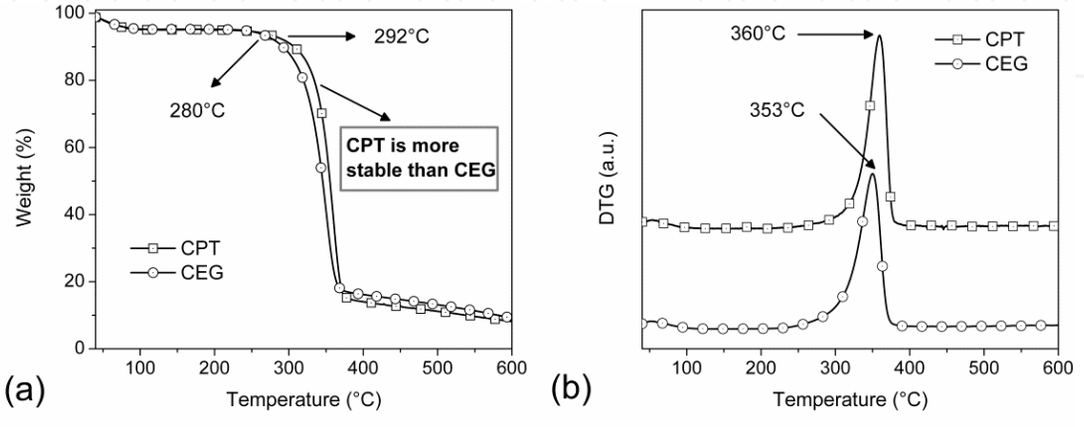

Figure 7. TGA (a) and DTG (b) curves of the cellulose samples studied.

5.4. Activation energy (E_a) in degradation

Figure 8 (A) shows the typical behavior of the thermal analysis conducted at different heating rates for the CPT sample while Figure 8 (B) illustrates the conversion curves determined from Equation (9).

In Figure 8, with the increase in heating rate, the curves show a shift to higher degradation temperatures, *i.e.*, there is a shorter time interval between the amount of heat supplied and absorbed by the sample. The observation of this behavior for the heating rate allows the use of the isoconversional method of Flynn-Wall-Ozawa (FWO) [19-22]. Figure 9 shows the linear fits from the plot of log β versus 1/T in the conversion range of 0.2-0.8 for the determination of the activation energy values obtained using the method proposed by FWO for the CPT sample. The linear fits showed correlation coefficient (r) values close to unity (minimum 0.9878 and maximum 0.9998) with a confidence interval of 95%. Figure 10 shows the activation energy values for the CEG and CPT samples in the conversion range of 0.2-0.8.

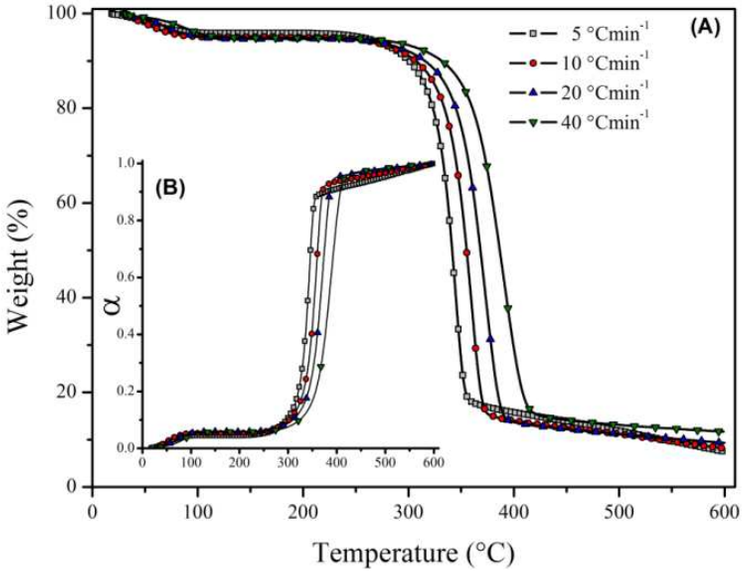

Figure 8. Thermogravimetric curves for several heating rates (A) and conversion curves (B) as a function of temperature for the CPT sample.

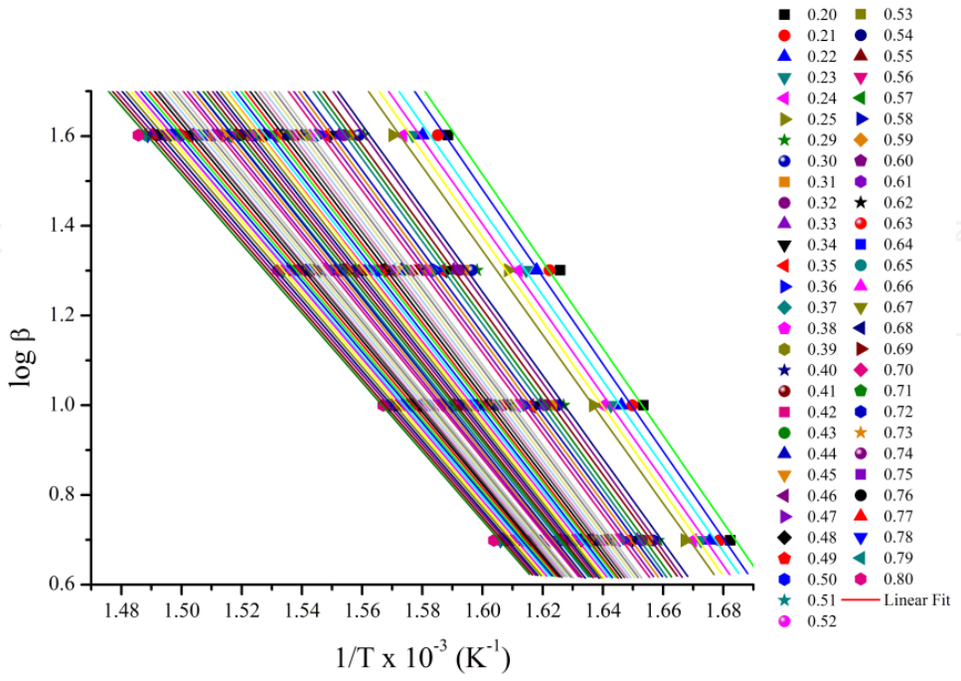

Figure 9. Linear fit determined by the conversion points trough different heating rates for the CPT sample using the FWO method.

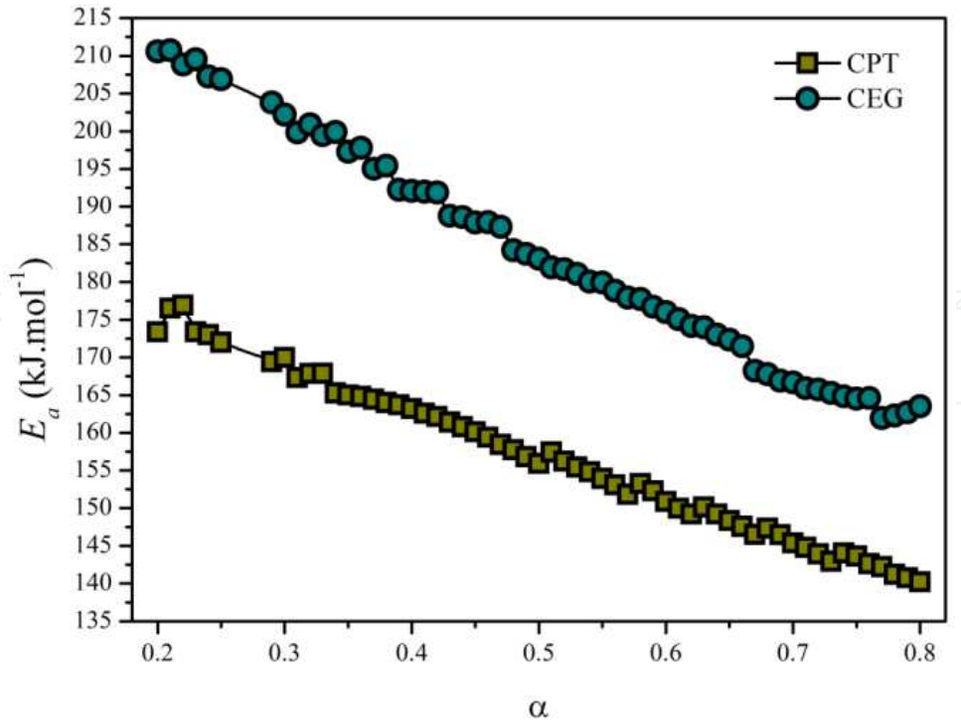

Figure 10. Activation energy values obtained trough the FWO method for both samples

In Figure 10 it is seen that the E_a values decrease progressively as the degradation process occurs for both celluloses studied. The activation energy E_a varies between 210-165 and 178-140 kJ/mol for the CEG and CPT samples, respectively. This range of values is consistent with the literature [35, 45-46]. The reduction in E_a is associated with the breaking of repeating units of ringed glucose molecules and molecular weight reduction of cellulose that may result from autocatalysis in the dehydration process [47]. Then, a mixed mechanism of depolymerization and dehydration can be considered for both pulp samples decomposition, regardless of the kind of pulp treatment. CEG sample exhibited larger values of activation energy than CPT. With respect to thermal stability, the crystal size, as shown in Table 3, may promote an increase in the degradation temperature [10, 21], and by consequence, the CPT cellulose fiber thermal stability may be higher than that of CEG. Moreover, the activation energy E_a value is not affected by the crystallite size [10] and therefore the lower E_a values observed for CPT can be attributed to the thermal decomposition of the sulfite pulp which can be controlled by dehydration, while the higher activation energy E_a values exhibited by CEG may indicate the depolymerization of kraft pulp with the production of levoglucosan [46-47]. Also, when considering the E_a values together with the data in Figure 6(b), the CPT sample showed a band in the 1642 cm^{-1} region, which is to be attributed to the adsorbed water in the cellulose structure in larger amount than in CEG. The higher amount of water adsorbed by the structure of CPT cellulose confirms the fact that the initiation of the CPT degradation can be more directly related to dehydration, which leads to lower activation energy E_a values. Similar behavior was observed by Soares et al. [47] for cellulose powder and kraft paper and by Scheirs et al. [48] for cellulose paper and kraft insulating paper.

Whereas different pulping conditions can affect the crystallinity of cellulose and differences in E_a suggest different relationships between the degradation mechanisms, it is also possible to evaluate the influence of different treatments on the structure of crystalline cellulose with the kinetic mechanism.

The activation energies E_a obtained using the FWO method were used to determine the degradation mechanisms proposed by Criado *et al*. [28]. This method uses reference theoretical curves obtained from Equation (19) that are derivatives of the $f(\alpha)$ and $g(\alpha)$ functions represented in Table 1. These theoretical curves are called master curves and are compared to experimental data obtained from Equation (20) for the determination of a solid-state process mechanism. These mechanisms represent how the solid-state degradation process occurs. The algebraic expressions that represent the theoretical mechanisms are separated into four groups, A_n, R_n, D_n and F_n, as can be seen in Table 1. These mechanisms describe processes of nuclei formation on the propagation of the degradation process; diffusion processes related to the heat transfer capacity along the material structure; reaction mechanisms controlled by the sample surface; and the random degradation of nuclei, respectively. To determine the $Z(\alpha)$ experimental values the heating rate (β) of 10 °Cmin^{-1} was used. The theoretical and experimental curves corresponding to these mechanisms are shown in Figure 11.

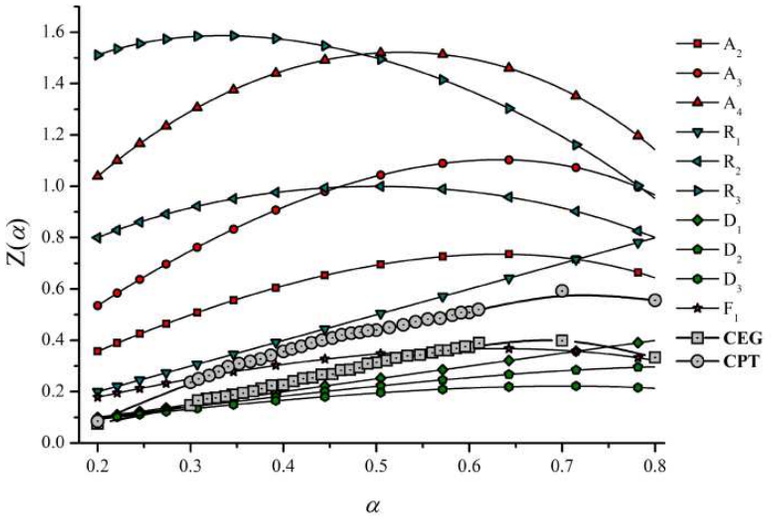

Figure 11. Master curves and experimental data obtained using the Criado method for both CPT and CEG samples.

The experimental data for the CEG sample in the conversion range of α = 0.2 - 0.4 overlapped on the D_n mechanism and according to the literature these degradation mechanisms refer to the diffusion processes in one, two and three dimensions, respectively [23, 28]. Similar results were described by Wu and Dollimore [49].As for the CPT sample, for α values in the range of 0.3 to 0.7 the degradation mechanism corresponded to R_1, *i.e.*, controlled reaction on the surface (motion in one dimension). The R_1 mechanism is also consistent with the results obtained from the XRD analysis, where the larger crystallite size for CPT might be related to the action of temperature on the boundaries due to the larger interfacial perimeter between crystals.

The degradation process is generally initiated in the cellulose amorphous regions, therefore, the smaller the size of the crystalline domains the larger number of amorphous regions which may be present in the structure of cellulose. So, in agreement with the lower crystallinity values found for the CEG sample from FTIR and XRD techniques this sample initiates the degradation process in the cellulose amorphous regions and when the conversion values are around 0.5 the CEG degradation mechanism tends towards F_1, corresponding to random nucleation with one individual particle nucleus. This behavior may be associated with the more pronounced degradation of the cellulose crystallite domains which results in the breakdown of the CEG crystallites and promotes random nucleation of the degradation process. As for CPT, of higher crystallite size, the degradation process is controlled by the degradation on the crystallites surface.

6. Conclusion

The crystallinity and kinetic decomposition of two cellulose samples obtained by two pulping processes were investigated. FTIR results indicated that CPT contains more cellulose chains in a highly organized form which may result in a more packed cellulose structure and higher crystallinity than CEG. Thermogravimetric results confirm that for the

CPT sample the thermal stability was higher than that of CEG probably due to the more ordered cellulose regions. In general, the crystallinity and thermal stability were more affected by the kraft pulping conditions than by those of sulfite pulping.

Through the kinetic parameters it was found that there are differences between the degradation processes of the cellulose fibers studied. For the CEG sample the degradation process occur by a diffusion process and probably starts in the cellulose amorphous domains while for CPT, which exhibits more crystalline regions than CEG, the more densely packed cellulose chains might hinder heat transfer by diffusion through the cellulose chains and then the degradation process may occur by degradation of the cellulose crystallites surface through a phase boundary-controlled reaction.

Science, technology, industry and government continue to move toward renewable, biodegradable, non-petroleum and carbon neutral raw materials. So, more environmentally friendly and sustainable resources and processes are desirable. Therefore, the demand for cellulose and cellulose derivatives is of growing importance in several applications as polymer materials, medical uses, food stuffs and in many other industry fields. However, from the discussion in this work it is obvious that the structure of cellulose is complex and the investigation of the many aspects of cellulose structure should be pursued to better understand this unique material.

Author details

Matheus Poletto* and Ademir J. Zattera
Laboratory of Polymers (LPOL), Center of Exact Sciences and Technology (CCET), University of Caxias do Sul (UCS), Caxias do Sul,RS, Brazil

Vinícios Pistor
Institute of Chemistry, Federal University of Rio Grande do Sul, UFRGS, Porto Alegre, RS, Brazil

Acknowledgement

The authors are grateful to Cambará S.A. and CMPC S.A. for supplying the cellulose samples. The authors also thank to CAPES and CNPq for financial support.

7. References

[1] O'Sullivan A (1997). Cellulose: the structure slowly unravels. Cellulose 4: 173-207.
[2] Klemm D, Heublein B, Fink H-P, Bohn A (2005). Cellulose: Fascinating Biopolymer and Sustainable Raw Material. Angew. Chem. Int. Ed. 44: 3358-3393.
[3] Moon RJ, Martini A, Nairn J, Simonsen J, Youngblood J (2011). Cellulose nanomaterials review: structure, properties and nanocomposites. Chem. Soc. Rev. 40: 3941-3994.

* Corresponding Author

[4] Bledzki AK, Gassan J (1999). Composites reinforced whit cellulose based fibres. Prog. Polym. Sci. 24: 221-274.
[5] Åkerholm M, Hinterstoisser B, Salmén L (2004). Characterization of the crystalline structure of cellulose using static and dynamic FT-IR spectroscopy. Carbohydr. Res. 339: 569-578.
[6] Oh SY, Yoo DI, Shin Y, Kim HC, Kim HY, Chung YS, Park WH, Youk JH (2005). Crystalline structure analysis of cellulose treated with sodium hydroxide and carbon dioxide by means of X-ray diffraction and FTIR spectroscopy. Carbohydr. Res. 340: 2376-2391.
[7] John MJ, Thomas, S (2008). Biofibres and biocomposites. Carbohydr. Polym. 71: 343-364.
[8] Gandini A (2011). The irruption of polymers from renewable resources on the scene of macromolecular science and technology. Green Chem. 13: 1061-1083.
[9] Hult E-I, Iversen T, Sugiyama J (2003). Characterization of the supermolecular structure of cellulose in wood pulp fibres. Cellulose 10: 103-110.
[10] Kim U-J, Eom SH, Wada M (2010). Thermal decomposition of native cellulose: Influence on crystallite size. Polym. Degrad. Stab. 95:778-781.
[11] Koyama M, Helbert W, Imai T, Sugiyama J, Henrissat B (1997). Parallel-up structure evidences the molecular directionality during biosynthesis of bacterial cellulose. Proc. Natl. Acad. Sci. 94: 9091-9095.
[12] Wada M, Chanzy H, Nishiyama Y, Langan P (2004). Cellulose III_I Crystal Structure and Hydrogen Bonding by Synchrotron X-ray and Neutron Fiber Diffraction. Macromolecules 37: 8548-8555.
[13] Wada M, Okano T (2001). Localization of I_α and I_β phases in algal cellulose revealed by acid treatments. Cellulose 8: 183-188.
[14] Popescu M-C, Popescu C-M, Lisa G, Sakata Y (2011). Evaluation of morphological and chemical aspects of different wood species by spectroscopy and thermal methods. J. Mol. Struct. 988: 65-72.
[15] Gümüskaya E, Usta M, Kirei H (2003). The effects of various pulping conditions on crystalline structure of cellulose in cotton linters. Polym. Degrad. Stab. 81: 559–564.
[16] Davidson TC, Newman RH, Ryan MJ (2004). Variations in the fibre repeat between samples of cellulose I from different sources. Carbohydr. Res. 339: 2889-2893.
[17] Carrilo F, Colom X, Suñol JJ, Saurina J (2004). Structural FTIR analysis and thermal characterization of lyocell and viscose-type fibres. Eur. Polym. J. 40: 2229-2234.
[18] Popescu C-M, Singurel G., Popescu M-C, Vasile C., Argyropoulos D.S., Willför S (2009). Vibrational spectroscopy and X-ray diffraction methods to establish the differences between hardwood and softwood. Carbohydr. Polym. 77: 851-857.
[19] Pistor V, Ornaghi FG, Fiorio R, Zattera AJ (2010). Thermal characterization of oil extracted from ethylene–propylene–diene terpolymer residues (EPDM).Thermochim. Acta 510: 93-96.
[20] Poletto M, Dettenborn J, Pistor V, Zeni M, Zattera AJ (2010). Materials produced from plant biomass. Part I: evaluation of thermal stability and pyrolysis of wood. Mat. Res. 13: 375-379.

[21] Poletto M, Pistor V, Zeni M, Zattera AJ (2011). Crystalline properties and decomposition kinetics of cellulose fibers in wood pulp obtained by two pulping process. Polym. Degrad. Stab. 96, 679-685.
[22] Bianchi O, Martins JDeN, Fiorio R, Oliveira RVB, Canto, LB (2011). Changes in activation energy and kinetic mechanism during EVA crosslinking. Polym. Test. 30: 616-624.
[23] Tiptipakorn S, Damrongsakkul S, Ando S, Hemvichian K, Rimdusi S (2007). Thermal degradation behaviors of polybenzoxazine and silicon-containing polyimide blends. Polym Degrad Stab 92: 1265–1278.
[24] Haines PJ (2002). Principles of thermal analysis and calorimetry. United Kingdom: RSC Paperbacks 238 p.
[25] Flynn JH, Wall LA (1966). General treatment of the thermogravimetry of polymers. Journal of Research of the National Bureau of Standards 70A: 487–523.
[26] Ozawa T (1966). A new method of quantitative differential thermal analysis. Bulletin of the Chemical Society of Japan 39: 2071–2085.
[27] Doyle CD (1961). Kinetic analysis of thermogravimetric data. J Appl Polym Sci 5: 285–292.
[28] Criado JM, Malek J, Ortega A (1989). Applicability of the master plots in kinetic analysis of non-isothermal data. Thermochim Acta 147: 377–385.
[29] Pérez-Maqueda LA, Criado, JM (2000). The accuracy of Senum and Yang's Approximations to the arrhenius integral. J. Therm. Anal. Calorim. 60: 909–915.
[30] Wada M, Okano T, Sugiyama J (2001). Allomorphs of native crystalline cellulose I evaluated by two equatorial d-spacings. J. Wood Sci. 47: 124-128.
[31] Howell CL (2008). Understanding wood biodegradation through the characterization of crystalline cellulose nanostructures. Doctoral thesis. University of Maine.
[32] Newman RH (2008). Simulation of X-ray diffractograms relevant to the purported polymorphs cellulose IV_I and IV_{II}. Cellulose 15: 769-778.
[33] Newman RH (1999). Estimation of the lateral dimensions of cellulose crystallites using ^{13}C NMR signal strengths. Solid State Nucl. Magn. Reson. 15: 21-29.
[34] Duchesne I, Hult EL, Molin U, Daniel G, Iversen T, Lennhon H (2001). The influence of hemicellulose on fibril-aggregation of kraft pulp fibres as revealed by FE-SEM and CP/MAS ^{13}C-NMR. Cellulose 8: 103-111.
[35] Nada AMA, Kamel S, El-Sakhawy M (2000). Thermal behavior and infrared spectroscopy of cellulose carbamates. Polym. Degrad. Stab. 70: 347-355.
[36] Quiévy N, Jacquet N, Sclavons M, Deroanne C, Paquot M, Devaux J (2010). Influence of homogenization and drying on the thermal stability of microfibrillated cellulose. Polym. Degrad. Stab. 95: 306-314.
[37] Adel MA, Abb El-Wahab ZH, Ibrahim AA, Al-Shemy MT (2011). Characterization of microcrystalline cellulose prepared from lignocellulosic materials. Part II: physicochemical properties. Carbohydr. Polym. 83: 676-687.
[38] Schwanninger M, Rodrigues JC, Pereira H, Hinterstoisser B (2004). Effects of short vibratory ball milling on the shape of FT-IR spectra of wood and cellulose. Vib. Spectrosc. 36: 23-40.

[39] Chen H, Ferrari C, Angiuli M, Yao J, Raspi C, Bramanti E (2010). Qualitative and quantitative analysis of wood samples by Fourier transform infrared spectroscopy and multivariate analysis. Carbohydr. Polym. 82: 772-778.
[40] Tserki V, Matzinos P, Kokkou S, Panayiotou C (2005). Novel biodegradable composites based on treated lignocellulosic waste flour as filler. Part I. Surface chemical modification and characterization of waste flour. Composites Part A. 36: 965-974.
[41] Corgié SC, Smith HM, Walker LP (2011). Enzymatic transformations of cellulose assessed by quantitative high-throughput Fourier transform infrared spectroscopy (QHT-FTIR). Biotechnol. Bioeng. 108: 1509-1520.
[42] Poletto M, Zattera AJ, Forte MMC, Santana RMC (2012). Thermal decomposition of wood: influence of wood components and cellulose crystallite size. Bioresour. Technol. 109: 148-153.
[43] Yang H, Yan R, Chen H, Zheng C, Lee DH, Liang DT (2006). In-depth investigation of biomass pyrolysis based on three major components: hemicellulose, cellulose and lignin. Energy Fuels. 20: 388-393.
[44] Bourbigot S, Chlebicki S, Mamleev V (2002). Thermal degradation of cotton under linear heating. Polym. Degrad. Stab. 78: 57-62.
[45] Antal MJ, Várhegyi G, Jakab E (1998). Cellulose pyrolysis kinetics: revisited. Ind. Eng. Chem. Res. 34: 1267–1275.
[46] Capart R, Khezami L, Burnham AK (2004). Assessment of various kinetic models for the pyrolysis of a microgranular cellulose. Thermochim. Acta. 417: 79–89.
[47] Soares S, Camino G, Levchik S (1995). Comparative study of the thermal decomposition of pure cellulose and pulp paper. Polym. Degrad. Stab. 49: 275–283.
[48] Scheirs J, Camino G, Tumiatti W (2001). Overview of water evolution during the thermal degradation of cellulose. Eur. Polym. J. 37: 933-942.
[49] Wu Y, Dollimore D (1998). Kinetic studies of thermal degradation of natural cellulosic materials. Thermochim. Acta. 324: 49–57.